Applied Thermal Engineering 251 (2024) 123385

Contents lists available at ScienceDirect

Applied Thermal Engineering

journal homepage: www.elsevier.com/locate/apthermeng

Research Paper

High-accuracy experimental study of performance characteristics of optimised Ranque-Hilsch vortex tube☆

Nafiz H.K. Chowdhury, Thomas Povey *

University of Oxford, Dept. Engineering Science, Parks Road, Oxford OX1 3PJ, UK

ARTICLE INFO

Keywords:
Ranque-Hilsch
Vortex tube
Refrigerator
Energy separation
Pressure ratio
Turbomachinery
Cooling

ABSTRACT

In this paper we present high-accuracy experimental measurements of the performance characteristics of an optimised Ranque-Hilsch vortex tube of cylindrical counter-flow design. Although this is a relatively mature research area, the published high-accuracy experimental data with quantified measurement uncertainty is very limited. The purpose is to provide a reference data-set for CFD method validation and calibration. The vortex tube design is a performance-optimum based on existing literature. We characterize the temperature separation, energy separation, efficiency, and coefficients of performance for three inlet pressures (3.0 bar, 5.0 bar and 7.0 bar) and for atmospheric back pressure. Performance characteristics are presented as a function of cold gas mass fraction. The lowest non-dimensional cold-exit temperature (normalised by inlet temperature) was 0.87, the highest coefficient of performance (decrease in enthalpy flux of the cold stream normalized by work needed to compress air to the inlet pressure) was 0.137, and the highest isentropic efficiency (ratio of the actual energy lost by cold stream to energy that would have been lost in an isentropic expansion of the entire inlet stream from the inlet pressure to the cold-exit pressure) was 0.16.

1. Introduction

The vortex tube is device that exploits viscous work and heat-transfer effects in high-speed swirling gas flows to achieve temperature separation between two outlet streams, when fed with a higher-pressure inlet stream. The concept is attributed to Ranque [1], who discovered the effect in the 1930 s. Vortex tubes have been extensively used [2] in industrial spot cooling, refrigeration systems (e.g. food processing, laboratory refrigeration), turbomachinery research (e.g. [3]), and hydrogen pre-cooling systems [4]. A variety of designs have been explored, the most common of which is the counter-flow cylindrical design. This is shown in Fig. 1.

Compressed working gas (typically air) is accelerated though a ring of tangential nozzles to high speed (often sonic or supersonic) so as to form a vortex within the vortex tube. In the vortex so-formed, it is observed that energy is transferred from lower to higher radius. This is thought to be due primarily due to viscous work effects (down a velocity gradient) with contributions (of negative sign) down a static temperature gradient. For higher-speed flow at the centre of the device, provided viscous work terms are significantly greater than conduction terms, this would lead to an increase in total temperature at the periphery and a decrease in total temperature at the centre (see Ranque [1], and Hilsch [5]). Accordingly, having allowed the temperature separation to develop, flow is stripped-off at the outer radius forming a hot stream, and at the centre, forming a cold stream. In a counter flow design (see Fig. 1) the hot-exit and cold-exit are at opposite ends of the tube. The cone valve, located at the hot-exit, controls both the mass flow of hot gas and, simultaneously, the operating pressure within the tube. Valve position therefore sets the cold-gas mass fraction, ε, defined by

$$\varepsilon = \frac{\dot{m}_c}{\dot{m}_1} \tag{1}$$

where $\dot{m}_c$ is the cold-exit mass flow rate and $\dot{m}_1$ is the inlet mass flow rate.

Vortex tube length to internal diameter (L/D_1) ratio is considered an important optimisation parameter. Early work by Hilsch [5] and Martynovskii and Alekseev [6] experimentally showed that for straight cylindrical vortex tubes, $L/D_1 = 50$ was optimal. Later studies (see, e.g. [7–9]) have given optimum L/D_1 in the range 20–55, with some dependence on the size of the cold orifice and the design of the inlet

☆ This document was produced by Thomas Povey on behalf of all authors (Nafiz Chowdhury and Thomas Povey).

* Corresponding author.
E-mail address: thomas.povey@eng.ox.ac.uk (T. Povey).

https://doi.org/10.1016/j.applthermaleng.2024.123385
Received 14 February 2024; Received in revised form 19 April 2024; Accepted 8 May 2024
Available online 11 May 2024
1359-4311/© 2024 The Authors. Published by Elsevier Ltd. This is an open access article under the CC BY-NC license (http://creativecommons.org/licenses/by-nc/4.0/).

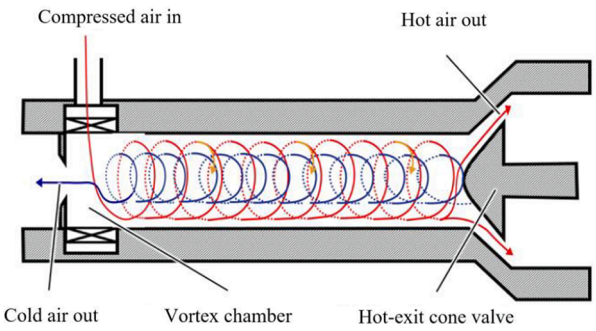


Fig. 1. Schematic of Ranque-Hilsch, vortex tube of cylindrical counter-flow design.

nozzle. Raiskii and Tunkel [7] observed that the main energy separation process takes place in the region closer to the tube inlet ($3 < L/D_1 < 5$). In our study we investigate a design with $L/D_1 = 20$, which seems to represent a good design compromise between achieving near-maximum energy separation and reasonable overall size.

The ratio of cold-exit orifice diameter to vortex tube internal diameter (d_c/D_1) has also been shown to affect performance. In experiments with cylindrical vortex tubes Saidi and Valipour [9], Nouri-Borujerdi [10] and Promvonge and Eiasma-ard [11] all concluded that maximum cold-exit temperature separation was achieved for $d_c/D_1 = 0.50$. Similar results have been found in computational studies: Liu and Liu [12] recommended 0.70. In our study we choose a diameter ratio $d_c/D_1 = 0.50$.

Inlet nozzle design and nozzle count (N) are found to influence the vortex tube performance. Gao [13] experimentally studied nozzle rings with 1, 2, 4 and 8 slots. He found that increasing the number of slots improved performance. In a later computational study, Behara et al. [8] explored both nozzle shape and nozzle count. They examined five configurations and found that vortex tubes with a higher number of nozzles ($N = 6$, in their study) produced the highest difference between hot-exit and cold-exit temperature. Gutsol [14] suggest a minimum requirement of four tangential nozzles to achieve uniform vortical flow. In our study we use a nozzle ring with six inlet nozzles.

Several studies [15–17] have investigated the influence of the ratio of nozzle ring total throat area to vortex tube internal cross-sectional area (A_1/A) on performance. Westley [17] developed an empirical correlation for optimum A_1/A as a function of inlet-total-pressure-to-cold-exit-static-pressure-ratio in the range $1.5 \le p_{01}/p_c \le 7.0$. This was

$$\frac{A_1}{A} = 0.156 + 0.176\left(\frac{p_{01}}{p_c}\right)^{-1} \tag{2}$$

For $p_{01}/p_c = 3.0$, this gives $A_1/A = 0.22$. In our study, we chose a nozzle aspect ratio of 0.22.

The shape of the hot exhaust valve has been shown to affect vortex tube performance. Pise and Devade [18] experimentally studied the effect the total included angle (φ) of a conical splitter valve at the hot exit, for a mildly divergent conical vortex tube with $d_c/D_1 = 0.50$; $A_1/A = 0.20$; $N = 2$; and $L/D_1 = 6$. The splitter valve angle was varied in the range $30^\circ < \varphi < 90^\circ$. Experiments were conducted over the inlet-total-pressure-to-cold-exit-static-pressure-ratio range $2.0 < p_{01}/p_c < 6.0$. The maximum cold-exit temperature separation occurred for $\varphi = 45°$; the maximum hot-exit temperature separation occurred for $\varphi = 60°$. Both results were for $p_{01}/p_c = 6.0$. Aydin and Baki [19] also experimentally evaluated tube performance for a range of splitter valve angles and pressure ratios. Fixed parameters were: $d_c/D_1 = 0.27$; $A_1/A = 0.20$; $L/D_1 = 19.44$. They investigated hot-exit cone-valve angles in the range $50^\circ \le \varphi \le 60^\circ$; pressure ratio was varied in the range $2.0 < p_{01}/p_c < 5.0$. They found maximum temperature separation occurred at $\varphi = 50^\circ$. Rafiee and Sadeghiazad [20] studied a tube with $d_c/D_1 = 0.50$, $L/D_1 = 13.9$, and $N = 2$, and tested a range of splitter valve angles between 20° and 80°. They observed the highest performance for $\varphi = 70°$ when $p_{01}/p_c = 4.0$. Conversely, Markal et al. [21] investigated the impact of splitter valve angles ($30^\circ < \varphi < 75^\circ$) across a broad range of L/D ratios with $d_c/D = 0.40$ and found that the valve angle had almost insignificant effect, particularly when L/D_1 exceeded 10. We choose $\varphi = 80°$ for our experiments (recalling that we chose $L/D_1 = 20$).

In this study we characterize the performance of the vortex tube as a function of inlet-total-pressure-to-cold-exit-static-pressure-ratio and the cold gas mass fraction.

Dincer et al. [22] studied the effect of pressure ratio in the range $1.5 < p_{01}/p_c < 4.0$, for a straight-cylindrical vortex tube with $d_c/D_1 = 0.55$, $A_1/A = 0.25$, $N = 4$ and $L/D_1 = 15$. They found that raising p_{01}/p_c above 3.8 did not result in significant performance enhancement (though they were near the top end of their range). This was in agreement with the results of Agrawal et al. [23] who found that cold-exit temperature separation increased with pressure ratio in the range of $3.0 < p_{01}/p_c < 5.0$, but the rate of increase was lower at higher pressure ratios. In our current study, we study performed for p_{01}/p_c values of 3.0, 5.0, and 7.0 [24].

Vortex tube performance is a strong function of cold-gas mass fraction (sets the general flow pattern within the tube), with many researchers finding maximum cold-exit temperature separation at approximately $\varepsilon = 0.30$, with maximum hot-exit temperature separation at around $\varepsilon = 0.80$. We study the full range of cold-gas mass fraction.

Although many studies have explored vortex tube performance in general, there are few studies which aim to comprehensively characterize performance curves for near-optimum vortex tube designs over a wide range of operating conditions. Fewer studies still provide detailed uncertainty quantification. Thus, there is limited data that could be used as a reference set for assessment of CFD models or for CFD calibration. The purpose of this paper is to provide high-accuracy performance data across a broad operating range for a near-optimum vortex tube.

2. Performance metrics

In this section we discuss the performance metrics for the vortex tube: non-dimensional temperatures; cold-gas and hot-gas energy separation parameters; definitions of isentropic efficiency; and a coefficient of performance. We consider the performance parameters to be functions of the cold-gas mass fraction, ε, and the overall pressure ratio, p_{01}/p_c.

2.1. Non-dimensional temperatures

We define non-dimensional cold and hot temperatures by

$$\theta_c\left(\varepsilon,\ \frac{p_{01}}{p_c}\right) = \frac{T_{0c}}{T_{01}} \tag{3}$$

and

$$\theta_h\left(\varepsilon,\ \frac{p_{01}}{p_c}\right) = \frac{T_{0h}}{T_{01}} \tag{4}$$

where T_{0c} and T_{0h} are the measured cold-exit and hot-exit temperatures, and T_{01} is the measured inlet temperature.

2.2. Non-dimensional cold-gas and hot-gas energy separation parameters

The energy transfer process between the cold and hot streams is thought to be primarily due to work done by viscous shear stress down the velocity gradient. We can define cold-gas and hot-gas energy separation parameters, E_c and E_h respectively, in which the energies lost by the cold stream and gained by the hot stream are normalised by the inlet enthalpy flux, giving

$$E_c\left(\varepsilon,\frac{p_{01}}{p_c}\right)=\frac{\dot{m}_c c_p(T_{01}-T_{0c})}{\dot{m}_1 c_p T_{01}}=\varepsilon(1-\theta_c) \tag{5}$$

and

$$E_h\left(\varepsilon,\frac{p_{01}}{p_c}\right)=\frac{\dot{m}_h c_p(T_{0h}-T_{01})}{\dot{m}_1 c_p T_{01}}=(1-\varepsilon)(\theta_h-1) \tag{6}$$

where $\dot{m}_h$ is hot-exit mass flow rate, c_p is specific heat capacity at constant pressure for air, and where all other parameters have been defined.

2.3. Definitions of isentropic efficiency

We can define isentropic efficiency in two ways (see also [24]). Firstly, the ratio of the actual energy lost by the cold stream to energy that would have been lost in isentropic expansion of the cold stream from the inlet pressure to the cold-exit pressure, that is

$$\eta_1\left(\varepsilon,\frac{p_{01}}{p_c}\right)=\frac{\dot{m}_c c_p(T_{01}-T_{0c})}{\dot{m}_c c_p T_{01}\left(1-\left(\frac{p_c}{p_{01}}\right)^{\frac{\gamma-1}{\gamma}}\right)}=\frac{1-\theta_c}{\left(1-\left(\frac{p_c}{p_{01}}\right)^{\frac{\gamma-1}{\gamma}}\right)} \tag{7}$$

where γ is the ratio of specific heat capacities for air $(\gamma=c_p/c_v)$. Secondly, the ratio of the actual energy lost by the cold stream to energy that would have been lost in an isentropic expansion of the *entire inlet stream* from the inlet pressure to the cold-exit pressure. That is

$$\eta_2\left(\varepsilon,\frac{p_{01}}{p_c}\right)=\frac{\dot{m}_c c_p(T_{01}-T_{0c})}{\dot{m}_1 c_p T_{01}\left(1-\left(\frac{p_c}{p_{01}}\right)^{\frac{\gamma-1}{\gamma}}\right)}=\frac{\varepsilon(1-\theta_c)}{\left(1-\left(\frac{p_c}{p_{01}}\right)^{\frac{\gamma-1}{\gamma}}\right)} \tag{8}$$

This second definition represents the efficiency with reference to an ideal turbo-expander.

2.4. Coefficient of performance as refrigerator

We can form a coefficient of performance (see also [24]) that measures the ratio between the decrease in enthalpy flux of the cold stream (refrigerating potential) and the work needed to compress the entire inlet stream from ambient conditions to the inlet pressure. A choice needs to be made about the type of compression (isentropic, adiabatic, isothermal etc). Taking the compression process to be isothermal (a common choice in the literature [25–27]) yields the lowest possible compression energy (for any typical real machine) and the highest possible COP. We write

$$\mathrm{COP}_c\left(\varepsilon,\frac{p_{01}}{p_c}\right)=\frac{\dot{m}_c c_p(T_{01}-T_{0c})}{\dot{m}_1 c_p\left(\frac{\gamma-1}{\gamma}\right)T_{01}\ln\left(\frac{p_{01}}{p_c}\right)}=\varepsilon\frac{\gamma}{\gamma-1}\frac{(1-\theta_c)}{\ln\left(\frac{p_{01}}{p_c}\right)} \tag{9}$$

3. Experimental setup

In this section we discuss practical details of the facility design and operation, the vortex tube design, and instrumentation and data acquisition. Details of the uncertainty analysis are given in the Appendix.

3.1. Facility design and operation

A schematic of the test facility is presented in Fig. 2. The facility operates from a large compressor system with intermediate air tanks (total volume 60 m^3) pressurized with dry air to 28.6 bar (all pressures are quoted absolute). Throughout the test, a pilot-operated pressure regulator was used to maintain a steady system inlet pressure ($p_{0,up}$) upstream of a critical venturi nozzle. The system inlet pressure is typically set in the range 10–15 bar. Mass flow can be varied independently

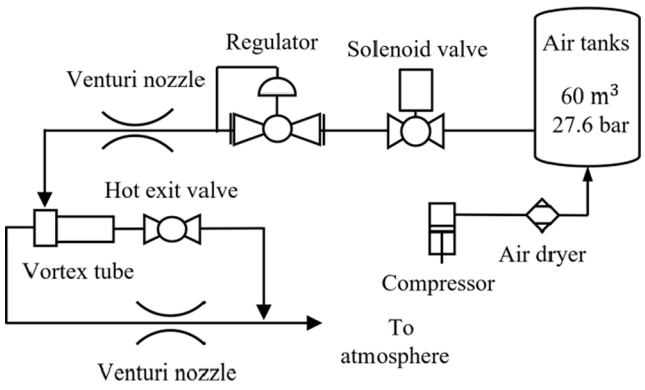


Fig. 2. Network schematic of the test facility.

of the set pressure by changing the nozzle size (typically in the diameter range $d_{nt}=5.5$–7.0 mm). This sets the inlet mass flow rate to the facility, $\dot{m}_1$, which—in turn—sets the nozzle ring inlet pressure, p_{01}. The test conditions in this study were arranged such that p_{01} was equal to 3.0, 5.0 and 7.0 bar. At the highest inlet pressure, the mass flow rate was approximately 0.10 kg/s. This is below the recharge rate of the compressors, so the system operates close to steady state at all times.

The cold outlet mass flow rate, $\dot{m}_c$, was measured using a subsonic venturi nozzle, with diameter chosen to minimise the backpressure increase (maintain p_c close to atmospheric pressure) whilst maintaining adequate pressure difference for accurate measurements. Diameters in the range 10–28 mm were used.

The hot-outlet mass flow rate, $\dot{m}_h$, was found by difference from the two measured mass flow rates: $\dot{m}_h=\dot{m}_1-\dot{m}_c$. The mass fraction was adjusted with a ball valve downstream of the hot outlet.

For a fixed vortex tube design (including hot-exit splitter design) and cold-exit nozzle diameter size, there is a well-defined relationship between the vortex tube operating pressures and two principal operating parameters (the cold gas mass fraction and the overall pressure ratio). That is, the functional forms for cold-exit nozzle downstream pressure and hot-exit static pressure (downstream of the splitter and upstream of the hot-exit ball valve) are: $p_c/p_{atm}=f(p_{01}/p_c,\varepsilon)$ and $p_h/p_{atm}=f(p_{01}/p_c,\varepsilon)$. In practice, the cold nozzle downstream pressure is extremely close to atmospheric pressure over the entire range of operating conditions. The vortex tube hot-exit static pressure increases with both cold-gas mass fraction and the overall pressure ratio. The particular characteristics are a function of the entire vortex tube design including the cold-exit limiter size and hot-exit splitter design. For more details see Cartledge et al. [24], and in practice (see [24]) this static pressure is relatively constant along the entire inner wall of the vortex tube. That is, the vortex tube operates at approximately constant peripheral static pressure throughout.

The vortex tube was covered with expanded polyethylene pipe insulation (13 mm thick) to minimize heat loss from the outer wall to the surrounding environment. Insultation reduced the maximum estimated heat loss from 1.0 % to 0.5 % of the energy separation.

3.2. Vortex tube design

A schematic representation of the vortex tube design is shown in Fig. 3.

Air is supplied from a regulated tank (Fig. 2) to inlet port A. This admits to a nozzle ring, B, which accelerates flow through six nozzles oriented in the radial-tangential plane, with the outlet flow in the tangential direction. At outlet the nozzles slots have 10:1 aspect ratio. The vortex tube has an internal diameter of 23 mm and can be configured to lave length-to-diameter ratios in the range $15<L/D_1<45$. The hot-end outlet, C, has a splitter valve with an angle $\varphi=80^\circ$. The outer diameter of the splitter valve, D_2, is larger than the tube diameter

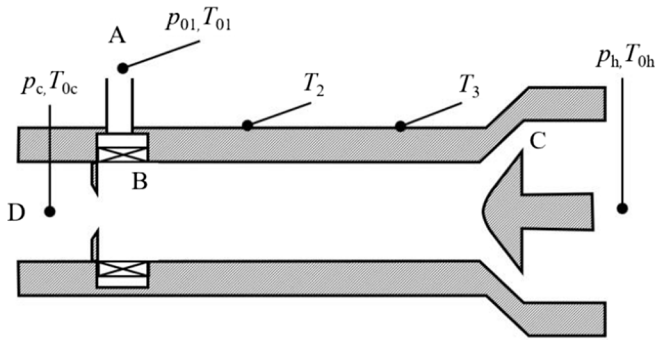


Fig. 3. Schematic of vortex tube and measurement points.

($D_2/D_1 = 1.52$). The cold-end outlet is through a limiting orifice that admits to outlet pipe D. A schematic of the nozzle ring and tube key dimensions are shown in Fig. 4. A summary of design parameters is given in Table 1.

3.3. Instrumentation and data acquisition

The system-inlet sonic venturi meter was installed with upstream total pressure and total temperature (K-type thermocouples) measurements and downstream static pressure tappings. The estimated bias errors for pressures and temperature were 0.10 % of full-scale (First Sensor CTE8000 0–35 bar) and approximately 1.0 K, respectively. All uncertainties are quoted to 95 % (2σ) confidence limits. Identical instruments were used for measurement of the nozzle ring upstream total pressure and total temperature (p_{01}, T_{01}).

The subsonic venturi downstream of the cold-exit was instrumented with upstream static pressure (Druck PMP-5000 0–2 bar) and total temperature measurements (K-type thermocouples) and a throat static pressure tapping (Druck PMP-5000 0–2 bar). The estimated bias errors for the absolute pressure sensors were 0.040 % of full-scale (0–2 bar). The thermocouple bias uncertainty was estimated to be 1.0 K.

The hot outlet temperature (T_{0h}) was measured approximately $1.5D_1$ downstream of the hot-exit plane using a rake of four K-type thermocouples. The estimated bias error for this measurement was 0.5 K.

The cold outlet total temperature (T_{0c}) and static pressure (p_c) were measured approximately $15d_c$ downstream of the cold orifice. A rake of four thermocouples was used for the temperature measurement (estimated bias error of 0.5 K). Pressure was measured with a First Sensor CTE8000 transducer (0–10 bar; estimated bias equal to 0.10 % of full-scale).

Data acquisition was performed using a Labview and National Instruments system with data sampled at 50 Hz in all experiments.

4. Transient heat flux correction

To account for heat flux between the working gas and the walls (to render the experiment closer to an adiabatic condition), two thermocouples (marked T_2 and T_3 in Fig. 3) were installed on the outer walls of the vortex tube. This allowed a zero-dimensional unsteady correction

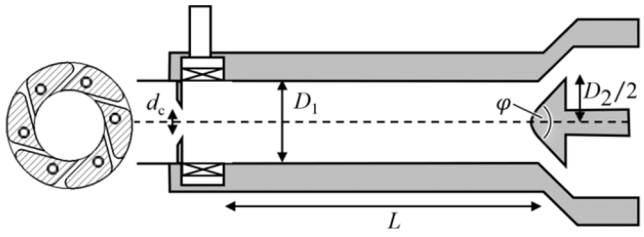


Fig. 4. Schematic of the vortex nozzle ring and tube, showing important dimensions.

Table 1
Summary of vortex tube dimensions.

Parameter	Value
Vortex tube internal diameter, D_1 (mm)	23
Angle of hot-exit conical splitter valve, φ (deg)	80
Number of inlet nozzles, N (–)	6
Ratio of (total) vortex nozzle ring throat area to vortex tube inlet internal cross-sectional area, A_1/A (–)	0.22
Ratio of cold-exit orifice plate diameter to vortex tube inlet diameter, d_c/D_1 (–)	0.50
Ratio of vortex tube length to inlet internal diameter, L/D_1 (–)	20
Ratio of conical splitter valve outer diameter to vortex tube diameter, D_2/D_1 (–)	1.52

method to be employed. Details of the method, and a discussion of the accuracy of the correction, are given in [24]. We briefly review the method here.

In Fig. 5 we shown corrected and uncorrected non-dimensional outlet temperature trends (with time), for an experiment of 600 s duration. Consider first the non-dimensional inlet temperature, normalized by its value at the start of the run: $T_{01}(t)/T_{01}(t = 0\ \text{s})$. By definition, at $t = 0$ this takes a value of unity. There is a mild temperature lapse during the experiment with $T_{01}(t)/T_{01}(t = 0\ \text{s}) = 0.99$ at the end of the run. This represents a drop of approximately 3 K during the course of the experiment.

Uncorrected non-dimensional hot-exit and cold-exit temperatures, $\theta_h = T_{0h}/T_{01}$ and $\theta_c = T_{0c}/T_{01}$, are also shown. For this particular run θ_h and θ_c take very approximate values 1.17 and 0.94 respectively. The uncorrected values have transient behaviour due to heat transfer, which is particularly pronounced in the first 200 s of the run. The corrected (using the zero-dimensional model) characteristics, θ'_h and θ'_c, are also shown. At 60 s, $\theta_h - 1$ and $1 - \theta_c$ deviate from their terminal values (evaluated at $t = 600$ s) by 7.5 % and 6.6 % respectively. In contrast, $\theta'_h - 1$ and $1 - \theta'_c$ deviate from their terminal values by 1.73 % and 2.33 % respectively. The in-practice unsteadiness residual is reduced to approximately 1/3 of its value when the correction method is employed.

It was assumed that 60 s dwell period at each condition was adequate when the unsteady correction method was employed. Throughout, we use prime notation to indicate variables that have been corrected for unsteady conduction effects: θ'_h, θ'_c, η'_1, η'_2, E'_h, E'_c and COP'_c.

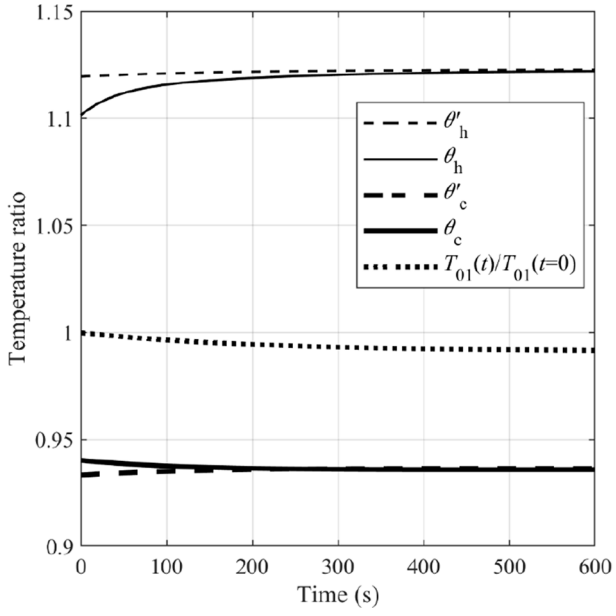


Fig. 5. Corrected and uncorrected non-dimensional exit temperatures after a step change in operating point to $p_{01}/p_c = 5.0$ and $\varepsilon = 0.60$.

5. Results and discussion

Performance characteristics are now presented for three overall total-to-static pressure ratios: $p_{01}/p_c = 3.0$, 5.0 and 7.0. We consider the following performance parameters: the non-dimensional outlet temperatures, θ'_c and θ'_h; the non-dimensional cold-gas and hot-gas energy separation, E'_c and E'_h; the isentropic efficiencies, η'_1 and η'_2; and the coefficient of performance of the vortex tube, COP'_c. All the non-dimensional performance parameters are corrected for transient heat flux. In all the characteristic plots that follow both raw data at individual operating points, and best-fit weighted cosine functions are presented. The estimated experimental uncertainty in the measurement of the performance parameters is presented in the Appendix.

In the calculation of performance parameters, the Joule-Thomson effect has *not* been separated. This is the most common way of presenting performance trends because it is the simplest way of presenting in-practice performance at particular conditions of inlet pressure. For scaling to conditions of different absolute pressure at the same pressure ratio, however, it would be necessary to separate the Joule-Thomson and vortex-tube effects. This is discussed in [24].

5.1. Non-dimensional cold-gas and hot-gas exit temperatures

Non-dimensional exit temperatures is shown in Fig. 6 as a function of cold-gas mass fraction, for pressure ratios $p_{01}/p_c = 3.0$, 5.0 and 7.0.

The non-dimensional cold-exit temperature minima were $\theta'_c = 0.90$, 0.88 and 0.87 for $p_{01}/p_c = 3.0$, 5.0 and 7.0, respectively. The minima were in the range $0.30 < \varepsilon < 0.40$. We note the significant performance improvement between pressure ratios 3.0 and 5.0, but only a modest change between 5.0 and 7.0. The experimental characteristics are similar to other experimental studies in the literature.

The non-dimensional hot-exit temperature maxima were $\theta'_h = 1.12$, 1.13 and 1.13 for $p_{01}/p_c = 3.0$, 5.0 and 7.0, respectively. Peak values occurred in the range $0.70 < \varepsilon < 0.90$. Increasing pressure ratio only slightly increased the hot gas temperature separation at the peak value. This was similar to the result in [24] for a mildly divergent vortex tube.

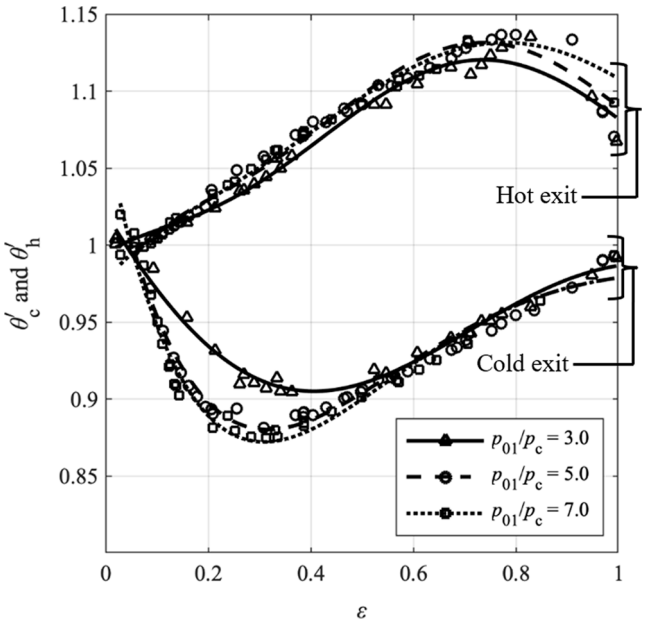


Fig. 6. Non-dimensional outlet temperatures as a function of ε and pressure ratio.

5.2. Non-dimensional cold-gas and hot-gas energy separation

Characteristics for cold-gas and hot-gas energy separation, E'_c and E'_h, are shown in Fig. 7 and Fig. 8 respectively. Mathematically these must be equal, $E'_c(\varepsilon, p_{01}/p_c) = E'_h(\varepsilon, p_{01}/p_c)$, and in an experiment we expect E'_c and E'_h to agree within uncertainty bands. For a given pressure ratio, the general form of the trends of E'_c and E'_h are very similar to each other, with similar peak values. Experimental uncertainties for E'_c are generally lower than those of E'_h in the range $0.10 < \varepsilon < 0.60$, with an average uncertainty of approximately 5.0 %. This explodes in the approach to $\varepsilon \to 0.00$ (increasing error in mass flow rate measurement). The average uncertainty in E'_h is approximately 9.7 % in the range of $0.60 < \varepsilon < 1.00$. For $p_{01}/p_c = 5.0$, the peak value of E'_c is 0.049 at $\varepsilon = 0.54$ where the corresponding value of E'_h is 0.047. The difference (approximately 4.0 %) is below the estimated error in E'_c and E'_h.

5.3. Isentropic efficiencies

Characteristics of isentropic efficiency referenced to an isentropic expansion of the cold stream (from the inlet pressure to the cold-exit pressure), η'_1, are shown in Fig. 9.

This is the ratio of actual energy separation compared to the enthalpy reduction associated with isentropic expansion of the cold-stream between inlet and cold-exit pressures. Peak efficiencies of $\eta'_1 = 0.36$, 0.35 and 0.31 were measured at pressure ratios of 3.0, 5.0, and 7.0, respectively, with corresponding values $\varepsilon = 0.37$, 0.31 and 0.30, respectively. The efficiency decreases slightly with increasing pressure ratio: whilst the energy separation goes up with increasing pressure ratio (see Fig. 7 and Fig. 8), the mass flow rate increases at a faster rate, increasing the hypothetical isentropic work term at faster rate.

Characteristics of isentropic efficiency referenced to an isentropic expansion of the inlet stream, (from the inlet pressure to the cold-exit pressure), η'_2, are shown in Fig. 10. Peak efficiencies of $\eta'_2 = 0.16$, 0.14, and 0.12 were measured at pressure ratios of 3.0, 5.0, and 7.0 respectively, with corresponding values $\varepsilon = 0.58$, 0.55 and 0.55, respectively. Because η'_2 is referenced to a hypothetical expansion of the entire inlet stream, the individual characteristic shapes are identical those for E'_c, but are scaled with respect to each other by a constant

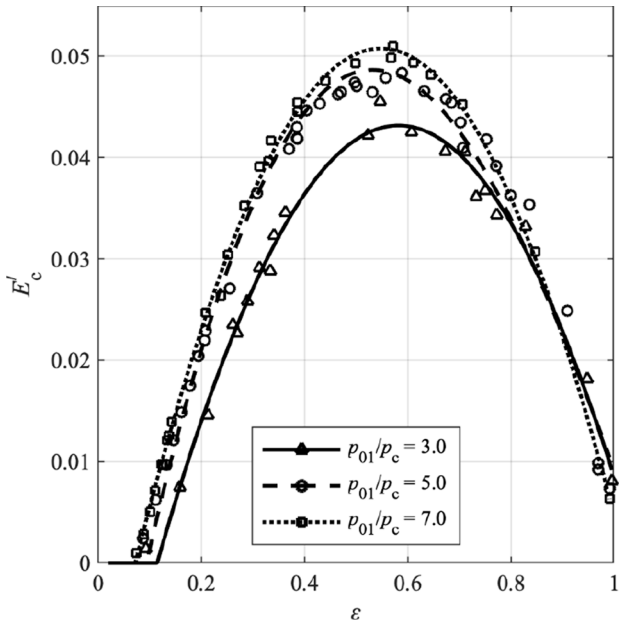


Fig. 7. Cold-gas energy separation parameter E'_c as a function of ε and pressure ratio.

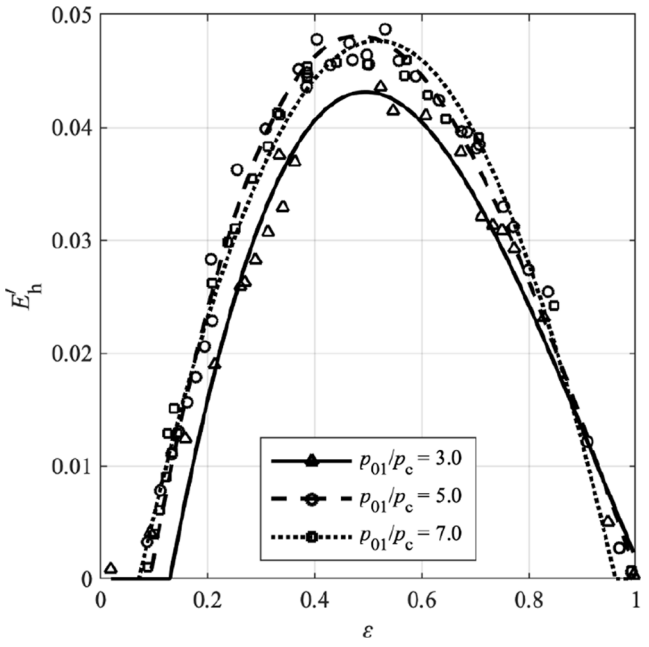


Fig. 8. Hot-gas energy separation parameter E'_h as a function of ε and pressure ratio.

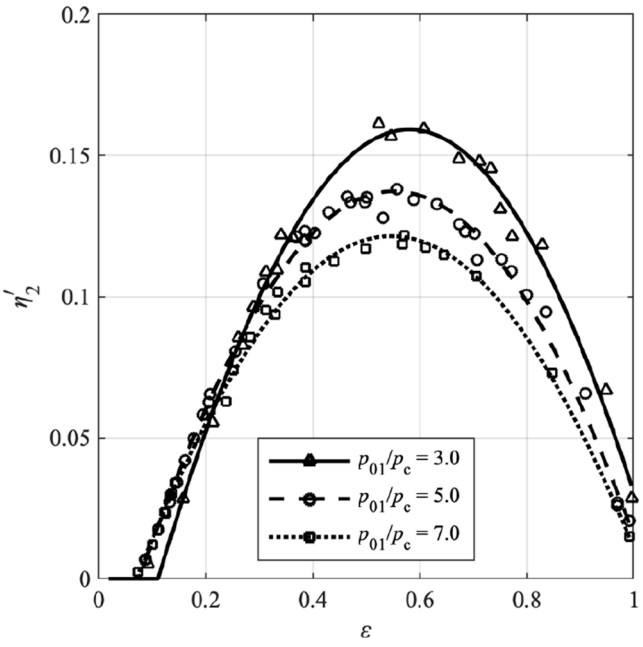


Fig. 10. Isentropic efficiency referenced to inlet-gas expansion, η'_2, as a function of ε and pressure ratio.

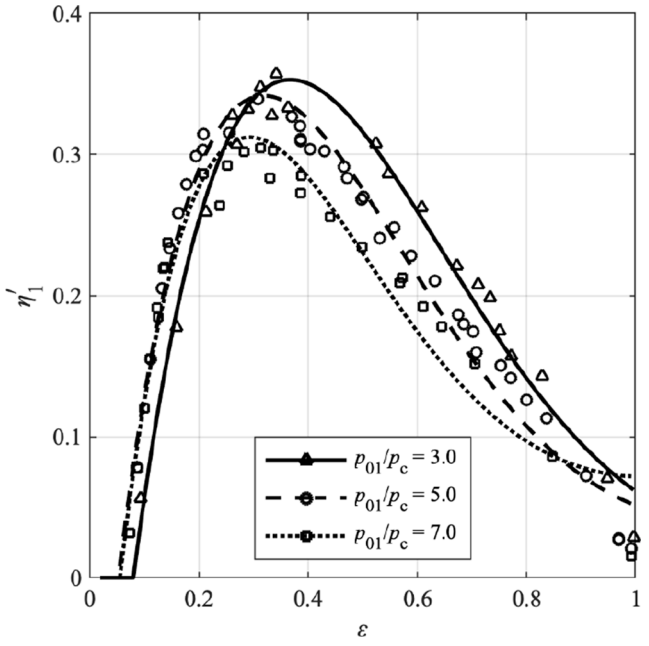


Fig. 9. Isentropic efficiency referenced to cold-gas expansion, η'_1, as a function of ε and pressure ratio.

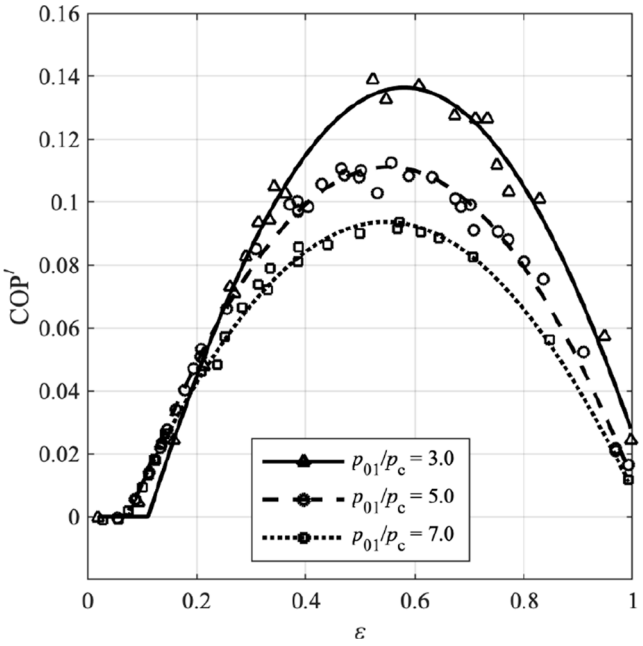


Fig. 11. Coefficient of performance acting as a refrigerator, COP'_c, as a function of ε and pressure ratio.

determined by the pressure ratio (see Eqs. (5) and (8), and Fig. 7).

5.4. Coefficient of performance as refrigerator

Characteristics of coefficient of performance, COP'_c, are presented in Fig. 11. Here we measure ratio between the decrease in enthalpy flux of the cold stream (refrigerating potential) and the work needed to compress the entire inlet stream from ambient conditions to the inlet pressure in an isothermal compression. At $\varepsilon = 0.00$, COP'_c is expected to be 0 since there is no mass flow from the cold exit and thus no refrigeration effect. This is true even when Joule-Thomson effects are not separated. Similarly, at $\varepsilon = 1.00$, COP'_c is expected to be 0—in the absence of Joule-Thomson effects—as there is no cold temperature separation. Small positive values are likely explained by a combination of experimental error (see Appendix) and the Joule-Thomson effect. Peak values of coefficient of performance of $COP'_c = 0.137$, 0.112, and 0.094 were measured at pressure ratios of 3.0, 5.0, and 7.0 respectively, with corresponding values $\varepsilon = 0.58$, 0.55 and 0.54 respectively. The refrigeration effect is approximately 14 % of the required compression work at peak performance.

6. Conclusions

We have presented a detailed high-accuracy experimental investigation of the performance characteristics of a Ranque-Hilsch vortex tube of cylindrical counter-flow design. The purpose is to provide a reference data-set for CFD method validation and calibration. The vortex tube design is a performance-optimum based on existing literature: $L/D_1 = 20$; $d_c/D_1 = 0.50$; $A_1/A = 0.215$; and $\varphi = 45°$. Experiments were performed at overall pressure ratios $p_{01}/p_c = 3.0$, 5.0 and 7.0 for the entire range of cold gas mass fraction using dry air as the working gas. We have attempted to be particularly careful with experimental method and error quantification to ensure the measured characteristics are as accurate as possible. We find that:

(a) Non-dimensional temperature separation (θ'_c, θ'_h) is greater with increasing overall pressure ratio. The minimum value of non-dimensional cold-gas temperature was $\theta'_c = 0.87$, which occurred for $p_{01}/p_c = 7.0$, and a cold-gas mass fraction of $\varepsilon = 0.31$. The maximum non-dimensional hot-gas temperature was $\theta'_h = 1.13$. This was achieved for both $p_{01}/p_c = 5.0$, and 7.0, at cold-gas mass fractions $\varepsilon = 0.73$ and 0.78 respectively. For ambient inlet temperature (290 K) these are equivalent to cold-gas and hot-gas temperature changes of −37.7 K and +37.7 K respectively.

(b) Non-dimensional cold-gas (E'_c) and hot-gas (E'_h) energy separation increased with increasing pressure ratio. Mathematically these must take the same value, but they were measured independently, with measurements of E'_c having lower error than measurements of E'_h. The two data agreed within errors, with a maximum value $E'_c = 0.051$ for $p_{01}/p_c = 7.0$ and $\varepsilon = 0.55$.

(c) The isentropic efficiency referenced to the cold stream expansion took a maximum value of $\eta'_1 = 0.36$ for $p_{01}/p_c = 3.0$ and $\varepsilon = 0.37$. The peak efficiency decreased slightly with increasing pressure ratio, reducing to $\eta'_1 = 0.31$ for $p_{01}/p_c = 7.0$. This reduction is explained by the fact that the additional inlet-stream compression work requirement at higher pressure ratio outweighs the increase in energy separation.

(d) The isentropic efficiency referenced to the inlet stream expansion took a maximum value of $\eta'_2 = 0.16$ for $p_{01}/p_c = 3.0$ and $\varepsilon = 0.58$. The peak efficiency decreased slightly with increasing pressure ratio, reducing to $\eta'_2 = 0.12$ for $p_{01}/p_c = 7.0$.

(e) The coefficient of performance (COP'_c) acting as a refrigerator took a maximum value of 0.137 for $p_{01}/p_c = 3.0$ and $\varepsilon = 0.58$. That is, the refrigeration effect is approximately 14 % of the required compression work at peak performance.

It is hoped that these data are of use for CFD validation and calibration in situations where Ranque-Hilsch vortex tubes are to be optimised for particular applications.

Nomenclature

A	Vortex tube inlet internal cross-sectional area, m^2
A_1	Total cross-sectional area of inlet nozzle throats, m^2
c_p	Specific heat capacity at constant pressure, J/(kg K)
C_d	Discharge coefficient, –
d_c	Cold-exit orifice plate diameter, m
D_1	Vortex tube internal diameter, m
D_2	Outer diameter of hot-exit conical splitter, m
E_c	Cold-gas energy separation parameter, –
E'_c	Cold-gas energy separation parameter, corrected for transient heat flux, –
E_h	Hot-gas energy separation parameter, –
E'_h	Hot-gas energy separation parameter, corrected for transient heat flux, –
L	Tube length, m
$\dot{m}_1$	Inlet mass flow rate, kg/s
$\dot{m}_c$	Cold-exit mass flow rate, kg/s
$\dot{m}_h$	Hot-exit mass flow rate, kg/s
N	Number of inlet nozzles, –
p	Static pressure, Pa
p_0	Total pressure, Pa
p_{01}	Inlet total pressure, Pa
p_{atm}	Atmospheric pressure, Pa
p_c	Cold-exit downstream static pressure, Pa
t	Time, s
T_0	Total temperature, K
T_{01}	Inlet total temperature, K
T_{0c}	Cold-exit total temperature, K
T'_{0c}	Cold-exit total temperature, corrected for transient heat flux, K
T_{0h}	Hot-exit total temperature, K
T'_{0h}	Hot-exit total temperature, corrected for transient heat flux, K
Greek Symbols	
ε	Cold gas mass fraction, –
η_1	Isentropic efficiency referenced to cold gas expansion, –
η'_1	Isentropic efficiency referenced to cold gas expansion, corrected for transient heat flux, –
η_2	Isentropic efficiency referenced to inlet stream expansion, –
η'_2	Isentropic efficiency referenced to inlet stream expansion, corrected for transient heat flux –
θ_c	Non-dimensional cold-exit total temperature, –
θ_h	Non-dimensional hot-exit total temperature, –
θ'_c	Non-dimensional cold-exit total temperature, corrected for transient heat flux, –
θ'_h	Non-dimensional hot-exit total temperature, corrected for transient heat flux, –
φ	Hot-exit conical splitter angle, degrees
Subscript	
0	Stagnation conditions
1,2,3	Station numbers
amb	Ambient conditions
c	Cold-exit conditions
h	Hot-exit conditions
nt	Nozzle throat conditions
up	Conditions upstream of venturi nozzle
Abbreviations	
COP_c	Coefficient of performance as refrigerator, –
COP'_c	Coefficient of performance as refrigerator, corrected for transient heat flux, –

CRediT authorship contribution statement

Nafiz H.K. Chowdhury: Writing – original draft. **Thomas Povey:** Writing – review & editing, Writing – original draft, Supervision, Project administration, Methodology, Formal analysis, Data curation, Conceptualization.

Declaration of competing interest

The authors declare that they have no known competing financial interests or personal relationships that could have appeared to influence the work reported in this paper.

Data availability

Data will be made available on request.

Acknowledgements

Daniel Burdett, Thomas Stewardson, Alessandro Bastianello, and Isaac Turner contributed variously to facility design, experimental work, and data analysis.

Appendix. Uncertainty analysis

Estimates of uncertainties in directly measured quantities and corrected temperatures are presented in Table 2. All uncertainties are quoted to 95 % (2σ) confidence limits. The source for these uncertainties is discussed the context of the experimental setup. Arbitrarily, we perform the analysis for a typical test with $p_{01}/p_c = 5.0$.

The uncertainties in the derived mass flows and cold-gas mass fraction ($\dot{m}_1$, $\dot{m}_c$, $\dot{m}_h$ and ε) and in the performance parameters (η_1', η_2', E_c', E_h' and COP_c') was calculated using root sum square error propagation assuming error were completely independent (this is true to a reasonable approximation). We calculate the uncertainties as a function of ε.

The uncertainties in $\dot{m}_1$, $\dot{m}_c$ and ε are shown as a function of ε in Fig. 12. The uncertainty in inlet mass flow rate, $\dot{m}_1$, was approximately 3.5 % and is independent of ε. The uncertainty in cold-exit mass flow rate, $\dot{m}_c$, is approximately constant at 2.3 % in the range $0.20 < \varepsilon \leq 1.0$, but increases rapidly for $\varepsilon < 0.20$ as the nozzle dynamic head becomes small in comparison to the full-scale range of the transducer. Steps in the characteristic are caused by subsonic venturi nozzle changes to keep measurements within the range of transducers.

The uncertainties in the performance parameters (η_1', η_2', E_c', E_h' and COP_c') are shown as a function of ε in Fig. 13. The uncertainty in η_1' (average value 0.21 for the range considered) has no sensitivity to mass flow or cold-gas mass fraction and has constant uncertainty of 5.0 %. Uncertainty characteristics for η_2', E_c' and COP_c' (average values of 0.10, 0.03 and 0.07 for the range considered, respectively) have similar characteristics to each other, linearly increasing between approximately 1.0 % and 15.0 % across the range $\varepsilon = 0.1$ to $\varepsilon = 1.0$. This is explained by their sensitivity coefficients being proportional to ε. The uncertainty in COP_c' increases faster with ε. The uncertainty profile of E_h' (average value of 0.03 for the data considered) is in the range 9–12 %. We have noted that E_c' and E_h' must be mathematically equivalent, but as a consequence of how they are—independently—measured, E_c' must be considered more accurate for $0.1 < \varepsilon < 0.6$, and E_h' more accurate for $\varepsilon > 0.5$. This is important in the reconciliation of the data in Fig. 7 and Fig. 8.

Table 2
Nominal values and estimated errors for directly measured variables for $p_{01}/p_c = 5.0$.

Parameter	Nominal value	Estimated bias error (2σ)	Estimated bias error (2σ)
		Sonic venturi	
C_d (–)	0.99	–	±0.30 %
d_{nt} (mm)	5.50	±0.1 mm	±1.8 %
$p_{0,up}$ (bar)	10	±0.035 bar	±0.35 %
$T_{0,up}$ (K)	287.0	±1.0 K	±0.35 %
		Subsonic venturi	
C_d	0.985	–	±2.0 %
d_{nt} (mm)	15.00	±0.1 mm	±0.67 %
p_{up} (bar)	1.065	±0.0008 bar	±0.08 %
p_{nt} (bar)	0.65–1.05	±0.0008 bar	0.08–0.12 %
$T_{0,up}$ (K)	267.0	±1.0 K	±0.37 %
		Vortex tube	
T'_{0c} (K)	265	±0.5 K	±0.19 %
p_c (bar)	1.065	±0.01 bar	±0.94 %
T_{01} (K)	290.0	±1.0 K	±0.35 %
p_{01} (bar)	5.00	±0.035 bar	±0.70 %
T'_{0h} (K)	317.0	±0.5 K	±0.16 %

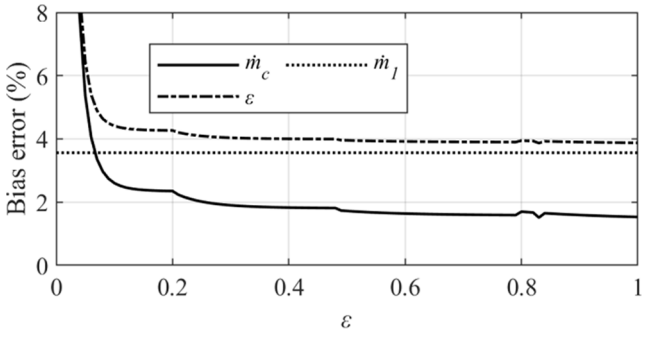


Fig. 12. Estimated percentage bias uncertainties for mass flow rates and ε, presented as a function of ε.

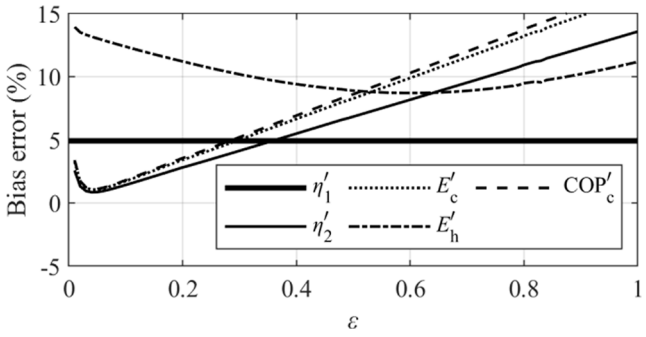


Fig. 13. Estimated percentage bias uncertainties for performance parameters, presented as a function of ε for $p_{01}/p_c = 5.0$.

References

[1] G. Ranque, Experiments on expansion in a vortex with simultaneous exhaust of hot air and cold air, Le Journal De Physique Et Le Radium (Paris) 4 (7) (1933) 112–114.

[2] S. Eiamsa-ard, P. Promvonge, Review of Ranque-Hilsch effects in vortex tubes, Renew. Sustain. Energy Rev. 12 (7) (2008) 1822–1842.

[3] S. Lewis, B. Barker, J.P. Bons, W. Ai, T.H. Fletcher, Film cooling effectiveness and heat transfer near deposit-laden film holes, ASME. J. Turbomach. 133 (3) (2010) 031003.

[4] W. Xu, Z. Yu, Q. Mu, B.P.Q. Li, Study of an integrated vortex tube used in hydrogen pre-cooling system, Int. J. Hydrogen Energy 54 (2024) 971–978.

[5] R. Hilsch, The use of the expansion of gases in a centrifugal field as cooling process, Rev. Sci. Instrum. 18 (2) (1947) 108–113.

[6] V.S. Martynovskii, V.P. Alekseev, Investigation of the vortex thermal separation effect for gases and vapors, Soviet Phys.-Techn. Phys. 1 (10) (1956) 2233–2243.

[7] Y. Raiskii, L. Tunkel, Influence of vortex-tube configuration and length on the process of energetic gas separation, J. Eng. Phys. 27 (1974) 1578–1581.

[8] U. Behera, P.J. Paul, S. Kasthurirengan, R. Karunanithi, S.N. Ram, K. Dinesh, S. Jacob, CFD analysis and experimental investigations towards optimizing the parameters of Ranque-Hilsch vortex tube, Int. J. Heat Mass Transf. 48 (10) (2005) 1961–1973.

[9] M. Saidi, M. Valipour, Experimental modelling of vortex tube refrigerator, Appl. Therm. Eng. 23 (15) (2003) 1971–1980.

[10] A. Nouri-Borujerdi, M. Bovand, S. Rashidi, K. Dincer, Geometric parameters and response surface methodology on cooling performance of vortex tubes, Int. J. Sustain. Energ. 36 (9) (2016) 872–886.

[11] P. Promvonge, S. Eiamsa-ard, Investigation on the vortex thermal separation in a vortex tube refrigerator, ScienceAsia 31 (2005) 215–223.

[12] X. Liu, Z. Liu, Investigation of the energy separation effect and flow mechanism inside a vortex tube, Appl. Therm. Eng. 67 (1–2) (2014) 494–506.

[13] C. Gao, Experimental Study on the Ranque-Hilsch Vortex, PhD Thesis, Technische Universiteit Eindhoven, 2005.

[14] A.F. Gutsol, The Ranque effect, Phys.-Usp. 40 (6) (1997) 639–658.

[15] H. Takahama, Studies on vortex tubes: (1) Experiments on efficiency of energy separation, (2) on profiles of velocity and temperature, Bull. JSME 8 (31) (1965) 433–440.

[16] M. Farzaneh-Gord, M. Sadi, Improving vortex tube performance based on vortex generator design, Energy 72 (2014) 492–500.

[17] R. Westley, Optimum Design of a Vortex Tube for Achieving Large Temperature Drop Ratios, *College of Aeronautics,* no. Cranfield College Note 30, (1955).

[18] A.T. Pise, K.D. Devade, Investigation of refrigeration effect using short divergent vortex tube, Int. J. Earth Sci. Eng. 5 (1) (2012) 378–384.

[19] O. Aydin, M. Baki, An experimental study on the design parameters of a counterflow vortex tube, Energy 31 (14) (2006) 2763–2772.

[20] S.E. Rafiee, M.M. Sadeghiazad, Effect of conical valve angle on cold-exit temperature of vortex tube, J. Thermophys Heat Transfer 28 (4) (2014) 785–794.

[21] B. Markal, O. Aydın, M. Avcı, An experimental study on the effect of the valve angle of counter-flow Ranque-Hilsch vortex tubes on thermal energy separation, Exp. Therm. Fluid Sci. 34 (7) (2010) 966–971.

[22] K. Dincer, S. Baskaya, B.Z. Uysal, I. Ucgul, Experimental investigation of the performance of a Ranque-Hilsch vortex tube with regard to a plug located at the hot outlet, Int. J. Refrig. 32 (2009) 87–94.

[23] N. Agrawal, S.S. Naik, Y.P. Gawale, Experimental investigation of vortex tube using natural substances, Int. Commun. Heat Mass Transfer 52 (2014) 51–55.

[24] J. Cartlidge, N. Chowdhury, T. Povey, Performance characteristics of a divergent vortex tube, Int. J. Heat Mass Transf. 186 (2022).

[25] J.R. Simões-Moreira, An air-standard cycle and a thermodynamic perspective on operational limits of Ranque-Hilsh or vortex tubes, Int. J. Refrig 33 (4) (2010) 765–773.

[26] E.S. Rafiee, Experimental and thermo-dynamical analysis of fully turbulent gas flows in vortex tube- fluid, temperature and power separations, isentropic efficiency, coefficient of performance (COP), Int. Commun. Heat Mass Transfer 138 (2022) 106296.

[27] M. Sadi, M. Farzaneh-Gord, Introduction of annular vortex tube and experimental comparison with Ranquee-Hilsch vortex tube, Int. J. Refrig 46 (2014) 142–151.